Ultrasound Imaging and its modeling

Jensen, Jørgen Arendt; Fink, M.; Kuperman, A.; Montagner, J-P.; Tourin, A.

Published in:
Imaging of Complex Media with Acoustic and Seismic Waves, Topics in Applied Physics

Publication date:
2002

Document Version
Early version, also known as pre-print

Preprint of:

Ultrasound imaging and its modeling

Chapter in. Fink et al. (Eds.): ”Imaging of Complex Media with Acoustic and Seismic Waves”, Topics in Applied Physics, vol. 84, pp. 135-165, Springer Verlag, 2002

Jørgen Arendt Jensen
Department of Information Technology, Build. 344
Technical University of Denmark,
DK-2800 Lyngby, Denmark

Published by Springer Verlag, 2002.

Contents

Chapter 1

Ultrasound imaging and its modeling

Modern medical ultrasound scanners are used for imaging nearly all soft tissue structures in the body. The anatomy can be studied from gray-scale B-mode images, where the reflectivity and scattering strength of the tissues are displayed. The imaging is performed in real time with 20 to 100 images per second. The technique is widely used, since it does not use ionizing radiation and is safe and painless for the patient.

This chapter gives a short introduction to modern ultrasound imaging using array transducers. It includes a description of the different imaging methods, the beamforming strategies used, and the resulting fields and their modeling.

1.1 Fundamental ultrasound imaging

The main units of a modern B-mode imaging system is shown in Fig. 1.1. A multi-element transducer is used for both transmitting and receiving the pulsed ultrasound field. The central frequency of the transducer can be from 2 to 15 MHz depending on the use. Often advanced composite materials are used in the transducer, and they can attain a relative bandwidth in excess of 100 %. The resolution is, thus, on the order of one to three wavelengths. The mean speed of sound in the tissue investigated varies from 1446 m/s (fat) to 1566 m/s (spleen) [1, 2], and an averaged value of 1540 m/s is used in the scanners. This gives an wavelength of 0.308 mm and a resolution in the axial direction of 0.3 to 1 mm.

The emission of the beam is controlled electronically as described in Section 1.3, and is for a phased array system swept over the region of interest in a polar scan. A single focus can be used in transmit, and the user can select the depth of the focus. The reflected and scattered field is then received by the transducer again and amplified by the time gain compensation amplifier. This compensates for the loss in amplitude due to the attenuation experienced during propagation of the sound field in the tissue. Typical attenuation values are shown in Table 1.1. A typical

value used, when designing the scanner, is 0.7 dB/[MHz·cm], indicating that the attenuation increases exponentially with both depth and frequency. This is the one-way attenuation and a 5 MHz wave measured at a depth of 10 cm would, thus, be attenuated 70 dB.

After amplification the signals from all transducer elements are passed to the electronic beamformer, that focuses the received beam. For low-end scanners this is done through analog delay lines, whereas more modern high-end scanners employ digital signal processing on a sampled version of the signal from all elements. Hereby a continuous focus can be attained giving a very high resolution image. Often the beamformer can handle 64 to 192 transducer elements, and this is the typical element count in modern scanners. There is a continuous effort to expand the number of channels to improve image resolution and contrast.

The beamformed signal is envelope detected and stored in a memory bank. A scan conversion is then performed to finally show the ultrasound image on a gray-level display in real time. The images can cover an area of 15 by 15 cm, and a single pulse-echo line then takes $2 \cdot 0.15/1540 = 195\mu$s to acquire. Since an image consists of roughly 100 polar lines, this gives a frame rate of 51 images a second. Often smaller images are selected to increase the frame rate, especially for blood velocity imaging [3].

A typical ultrasound image is shown in Fig. 1.2 for a fetus in the 13th week. The head, mouth, legs and the spine is clearly identified in the image. It is also seen that the image has a grainy appearance, and that there are no clear demarcations or reflection between the placenta and the amniotic fluid surrounding the fetus. There are, thus, no distinct reflections from plane boundaries as they seldom exist in the body. It is the ultrasound field scattered by the constituents of the tissue that is displayed in medical ultrasound, and the medical scanners are optimized to display the scattered signal. The scattered field emanates from small changes in density, compressibility, and absorption from the connective tissue, cells, and fibrous tissue. These structures are much smaller than one wavelength of the ultrasound, and the resulting speckle pattern displayed does not directly reveal physical structure. It is rather the constructive and destructive interference of scattered signals from all the small structures. So it is not possible to visualize and diagnose microstructure, but the strength of the signal is an indication of pathology. A strong signal from liver tissue, making a bright image, is, *e.g.*, an indication of a fatty or cirrhotic liver.

As the scattered wave emanates from numerous contributors, it is appropriate to characterize it in statistical terms. The amplitude distribution follows a Gaussian distribution [4], and is, thus, fully characterized by its mean and variance. The mean value is zero since the scattered signal is generated by differences in the tissue from the mean acoustic properties.

Since the backscattered signal depends on the constructive and destructive interference of waves from numerous small tissue structures, it is not meaningful to talk about the reflection strength of the individual structures. Rather, it is the deviations from the mean density and speed of sound within the tissue and the composition of the tissue that determine the strength of the returned signal. The magnitude of the returned signal is, therefore, described in terms of the

power of the scattered signal. Since the small structures re-radiate waves in all directions and the scattering structures might be ordered in some direction, the returned power will, in general, be dependent on the relative position between the ultrasound emitter and receiver. Such a medium is called anisotropic, examples of which are muscle and kidney tissue. By comparison, liver tissue is a fairly isotropic scattering medium, when its major vessels are excluded, and so is blood.

1.2 Imaging with arrays

Basically there are three different kinds of images acquired by multi-element array transducers, *i.e.* linear, convex, and phased as shown in Figures 1.3, 1.5, and 1.6. The linear array transducer is shown in Fig. 1.3. It selects the region of investigation by firing a set of elements situated over the region. The beam is moved over the imaging region by firing sets of contiguous elements. Focusing in transmit is achieved by delaying the excitation of the individual elements, so an initially concave beam shape is emitted, as shown in Fig. 1.4.

The beam can also be focused during reception by delaying and adding responses from the different elements. A continuous focus or several focal zones can be maintained as explained in Section 1.3. Only one focal zone is possible in transmit, but a composite image using a set of foci from several transmissions can be made. Often 4 to 8 zones can be individually placed at selected depths in modern scanners. The frame rate is then lowered by the number of transmit foci.

The linear arrays acquire a rectangular image, and the arrays can be quite large to cover a sufficient region of interest (ROI). A larger area can be scanned with a smaller array, if the elements are placed on a convex surface as shown in Fig. 1.5. A sector scan is then obtained. The method of focusing and beam sweeping during transmit and receive is the same as for the linear array, and a substantial number of elements (often 128 or 256) is employed.

The convex and linear arrays are often too large to image the heart when probing between the ribs. A small array size can be used and a large field of view attained by using a phased array as shown in Fig. 1.6. All array elements are used here both during transmit and receive. The direction of the beam is steered by electrically delaying the signals to or from the elements, as shown in Fig. 1.4b. Images can be acquired through a small window and the beam rapidly sweeped over the ROI. The rapid steering of the beam compared to mechanical transducers is of especial importance in flow imaging [3]. This has made the phased array the choice for cardiological investigations through the ribs.

More advanced arrays are even being introduced these years with the increase in number of elements and digital beamforming. Especially elevation focusing (out of the imaging plane) is important. A curved surface as shown in Fig. 1.7 is used for obtaining the elevation focusing essential for an improved image quality. Electronic beamforming can also be used in the ele-

vation direction by dividing the elements in the elevation direction. The elevation focusing in receive can then be dynamically controlled for *e.g.* the array shown in Fig. 1.8.

1.3 Focusing

The essence of focusing an ultrasound beam is to align the pressure fields from all parts of the aperture to arrive at the field point at the same time. This can be done through either a physically curved aperture, through a lens in front of the aperture, or by the use of electronic delays for multi-element arrays. All seek to align the arrival of the waves at a given point through delaying or advancing the fields from the individual elements. The delay (positive or negative) is determined using ray acoustics. The path length from the aperture to the point gives the propagation time and this is adjusted relative to some reference point. The propagation time t_i from the center of the aperture element to the field point is

$$t_i = \frac{1}{c}\sqrt{(x_i - x_f)^2 + (y_i - y_f)^2 + (z_i - z_f)^2} \tag{1.1}$$

where (x_f, y_f, z_f) is the position of the focal point, (x_i, y_i, z_i) is the center for the physical element number i, and c is the speed of sound.

A point is selected on the whole aperture as a reference for the imaging process. The propagation time for this is

$$t_c = \frac{1}{c}\sqrt{(x_c - x_f)^2 + (y_c - y_f)^2 + (z_c - z_f)^2} \tag{1.2}$$

where (x_c, y_c, z_c) is the reference center point on the aperture. The delay to use on each element of the array is then

$$\Delta t_i = \frac{1}{c}\left(\sqrt{(x_c - x_f)^2 + (y_c - y_f)^2 + (z_c - z_f)^2} - \sqrt{(x_i - x_f)^2 + (y_i - y_f)^2 + (z_i - z_f)^2}\right) \tag{1.3}$$

Notice that there is no limit on the selection of the different points, and the beam can, thus, be steered in a preferred direction.

The arguments here have been given for emission from an array, but they are equally valid during reception of the ultrasound waves due to acoustic reciprocity. At reception it is also possible to change the focus as a function of time and thereby obtain a dynamic tracking focus. This is used by all modern ultrasound scanners, Beamformers based on analog technology makes it possible to create several receive foci and the newer digital scanners change the focusing continuously for every depth in receive.

The focusing can, thus, be defined through time lines as:

From time	Focus at
0	x_1, y_1, z_1
t_1	x_1, y_1, z_1
t_2	x_2, y_2, z_2
$\vdots$	$\vdots$

For each focal zone there is an associated focal point and the time from which this focus is used. The arrival time from the field point to the physical transducer element is used for deciding which focus is used. Another possibility is to set the focusing to be dynamic, so that the focus is changed as a function of time and thereby depth. The focusing is then set as a direction defined by two angles and a starting point on the aperture.

Section 1.4 shows that the side and grating lobes of the array can be reduced by employing apodization of the elements. Again a fixed function can be used in transmit and a dynamic function in receive defined by:

From time	Apodize with
0	$a_{1,1}, a_{1,2}, \cdots a_{1,N_e}$
t_1	$a_{1,1}, a_{1,2}, \cdots a_{1,N_e}$
t_2	$a_{2,1}, a_{2,2}, \cdots a_{2,N_e}$
t_3	$a_{3,1}, a_{3,2}, \cdots a_{3,N_e}$
$\vdots$	$\vdots$

Here $a_{i,j}$ is the amplitude scaling value multiplied onto element j after time instance t_i. Typically a Hamming or Gaussian shaped function is used for the apodization. In receive the width of the function is often increased to compensate for attenuation effects and for keeping the point spread function roughly constant. The F-number defined by

$$F = \frac{D}{L} \tag{1.4}$$

where L is the total width of the active aperture and D is the distance to the focus, is often kept constant. More of the aperture is often used for larger depths and a compensation for the attenuation is thereby partly made. An example of the use of dynamic apodization is given in Section 1.7.

1.4 Ultrasound fields

This section derives a simple relation between the oscillation of the transducer surface and the ultrasound field. It is shown that field in the far-field can be found by a simple one-dimensional

Fourier transform of the one-dimensional aperture pattern. This might seem far from the actual imaging situation in the near field using pulsed excitation, but the approach is very convenient in introducing all the major concepts like main and side lobes, grating lobes, etc. It also very clearly reveals information about the relation between aperture properties and field properties.

1.4.1 Derivation of Fourier relation

Consider a simple line source of length L as shown in Fig. 1.9 with a harmonic particle speed of $U_0 \exp(j\omega t)$. Here U_0 is the vibration amplitude and ω is its angular frequency. The line element of length dx generates an increment in pressure at r' of [5]

$$dp = j\frac{\rho_0 ck}{4\pi r'} U_0 a_p(x) e^{j(\omega t - kr')} dx, \tag{1.5}$$

where ρ_0 is density, c is speed of sound, $k = \omega/c$ is the wavenumber, and $a_p(x)$ is an amplitude scaling of the individual parts of the aperture. In the far-field $(r \gg L)$ the distance from the radiator to the field points is (see Fig. 1.9):

$$r' = r - x\sin\theta \tag{1.6}$$

The emitted pressure is found by integrating over all the small elements of the aperture

$$p(r,\theta,t) = j\frac{\rho_0 cU_0 k}{4\pi}\int_{-\infty}^{+\infty} a_p(x)\frac{e^{j(\omega t - kr')}}{r'}dx. \tag{1.7}$$

Notice that $a_p(x) = 0$ if $|x| > L/2$. Here r' can be replaced with r, if the extent of the array is small compared to the distance to the field point $(r \gg L)$. Using this approximation and inserting (1.6) in (1.7) gives

$$p(r,\theta,t) = j\frac{\rho_0 cU_0 k}{4\pi r}\int_{-\infty}^{+\infty} a_p(x) e^{j(\omega t - kr + kx\sin\theta)}dx = j\frac{\rho_0 cU_0 k}{4\pi r} e^{j(\omega t - kr)}\int_{-\infty}^{+\infty} a_p(x) e^{jkx\sin\theta}dx, \tag{1.8}$$

since ωt and kr are independent of x. Hereby the pressure amplitude of the field for a given frequency can be split into two factors:

$$\begin{aligned} P_{ax}(r) &= \frac{\rho_0 cU_0 kL}{4\pi r} \\ H(\theta) &= \frac{1}{L}\int_{-\infty}^{+\infty} a_p(x) e^{jkx\sin\theta}dx \\ P(r,\theta) &= P_{ax}(r)H(\theta) \end{aligned} \tag{1.9}$$

The first factor $P_{ax}(r)$ characterizes how the field drops off in the axial direction as a factor of distance, and $H(\theta)$ gives the variation of the field as a function of angle. The first term drops

off with $1/r$ as for a simple point source and $H(\theta)$ is found from the aperture function $a_p(x)$. A slight rearrangement gives[1]

$$H(\theta) = \frac{1}{L}\int_{-\infty}^{+\infty} a_p(x) e^{j2\pi x f \frac{\sin\theta}{c}} dx = \frac{1}{L}\int_{-\infty}^{+\infty} a_p(x) e^{j2\pi x f'} dx. \tag{1.10}$$

This very closely resembles the standard Fourier integral given by

$$\begin{aligned} G(f) &= \int_{-\infty}^{+\infty} g(t) e^{-j2\pi t f} dt \\ g(t) &= \int_{-\infty}^{+\infty} G(f) e^{j2\pi t f} df \end{aligned} \tag{1.11}$$

There is, thus, a Fourier relation between the radial beam pattern and the aperture function, and the normal Fourier relations can be used for understanding the beam patterns for typical apertures.

1.4.2 Beam patterns

The first example is for a simple line source, where the aperture function is constant such that

$$a_p(x) = \begin{cases} 1 & |x| \le L/2 \\ 0 & \text{else} \end{cases} \tag{1.12}$$

The angular factor is then

$$H(\theta) = \frac{\sin(\pi L f \frac{\sin\theta}{c})}{\pi L f \frac{\sin\theta}{c}} = \frac{\sin(\frac{k}{2} L \sin\theta)}{\frac{k}{2} L \sin\theta} \tag{1.13}$$

A plot of the sinc function is shown in Fig. 1.10. A single main lobe can be seen with a number of side lobe peaks. The peaks fall off proportionally to k or f. The angle of the first zero in the function is found at

$$\sin\theta = \frac{c}{Lf} = \frac{\lambda}{L}. \tag{1.14}$$

The angle is, thus, dependent on the frequency and the size of the array. A large array or a high emitted frequency, therefore, gives a narrow main lobe.

The magnitude of the first sidelobe relative to the mainlobe is given by

$$\frac{H(\arcsin(\frac{3c}{2Lf}))}{H(0)} = L\frac{\sin(3\pi/2)}{3\pi/2}/L = \frac{2}{3\pi} \tag{1.15}$$

[1]The term $1/L$ is included to make $H(\theta)$ a unit less number.

The relative sidelobe level is, thus, independent of the size of the array and of the frequency, and is solely determined by the aperture function $a_p(x)$ through the Fourier relation. The large discontinuities of $a_p(x)$, thus, give rise to the high side lobe level, and they can be reduced by selecting an aperture function that is smoother like a Hanning window or a Gaussian shape.

Modern ultrasound transducers consist of a number of elements each radiating ultrasound energy. Neglecting the phasing of the element (see Section 1.3) due to the far-field assumption, the aperture function can be described by

$$a_p(x) = a_{ps}(x) * \sum_{n=-N/2}^{N/2} \delta(x - d_x n), \tag{1.16}$$

where $a_{ps}(x)$ is the aperture function or apodization for the individual elements, d_x is the spacing (pitch) between the centers of the individual elements, and $N+1$ is the number of elements in the array. Using the Fourier relationship the angular beam pattern can be described by

$$H_p(\theta) = H_{ps}(\theta) H_{per}(\theta), \tag{1.17}$$

where

$$\sum_{n=-N/2}^{N/2} \delta(x - d_x n) \leftrightarrow H_{per}(\theta) = \sum_{n=-N/2}^{N/2} e^{-jnd_x k \sin\theta} = \sum_{n=-N/2}^{N/2} e^{-j2\pi \frac{f \sin\theta}{c} n d_x}. \tag{1.18}$$

Summing the geometric series gives

$$H_{per}(\theta) = \frac{\sin\left((N+1)\frac{k}{2} d_x \sin\theta\right)}{\sin\left(\frac{k}{2} d_x \sin\theta\right)}, \tag{1.19}$$

which is the Fourier transform of a series of delta functions. This function repeats itself with a period that is a multiple of

$$\begin{aligned} \pi &= \frac{k}{2} d_x \sin\theta \\ \sin\theta &= \frac{2\pi}{k d_x} = \frac{\lambda}{d_x}. \end{aligned} \tag{1.20}$$

This repetitive function gives rise to the grating lobes in the field. An example is shown in Fig. 1.11. The grating lobes are due to the periodic nature of the array, and corresponds to sampling of a continuous time signal. The grating lobes will be outside a ± 90 deg. imaging area if

$$\begin{aligned} \frac{\lambda}{d_x} &= 1 \\ d_x &= \lambda \end{aligned} \tag{1.21}$$

Often the beam is steered in a direction and in order to ensure that grating lobes do not appear in the image, the spacing or pitch of the elements is selected to be $d_x = \lambda/2$. This also includes ample margin for the modern transducers that often have a very broad bandwidth.

An array beam can be steered in a direction by applying a time delay on the individual elements. The difference in arrival time between elements for a given direction θ_0 is

$$\tau = \frac{d_x \sin\theta_0}{c} \tag{1.22}$$

Steering in a direction θ_0 can, therefore, be accomplished by using

$$\sin\theta_0 = \frac{c\tau}{d_x} \tag{1.23}$$

where τ is the delay to apply to the signal on the element closest to the center of the array. A delay of 2τ is then applied on the second element and so forth. The beam pattern for the grating lobe is then replaced by

$$H_{per}(\theta) = \frac{\sin\left((N+1)\frac{k}{2}d_x\left(\sin\theta - \frac{c\tau}{d_x}\right)\right)}{\sin\left(\frac{k}{2}d_x\left(\sin\theta - \frac{c\tau}{d_x}\right)\right)}. \tag{1.24}$$

Notice that the delay is independent of frequency, since it is essentially only determined by the speed of sound.

1.5 Spatial impulse responses

The description in the last section is strictly only valid for the far-field, continuous wave case, whereas the fields employed in medical ultrasound are pulsed and in the near field. A more accurate and general solution is, thus, needed, and this is developed in this section. The approach is based on the concept of spatial impulse responses developed by Tupholme [6] and Stepanishen [7, 8].

1.5.1 Fields in linear acoustic systems

It is a well known fact in electrical engineering that a linear electrical system is fully characterized by its impulse response. Applying a delta function to the input of the circuit and measuring its output characterizes the system. The output $y(t)$ to any kind of input signal $x(t)$ is then given by

$$y(t) = h(t) * x(t) = \int_{-\infty}^{+\infty} h(\theta)x(t-\theta)d\theta, \tag{1.25}$$

where $h(t)$ is the impulse response of the linear system and $*$ denotes time convolution. The transfer function of the system is given by the Fourier transform of the impulse response and characterizes the systems amplification of a time-harmonic input signal.

The same approach can be taken to characterize a linear acoustic system. The basic set-up is shown in Fig. 1.12. The acoustic radiator (transducer) on the left is mounted in a infinite, rigid baffle and its position is denoted by $\vec{r}_2$. It radiates into a homogeneous medium with a constant speed of sound c and density ρ_0 throughout the medium. The point denoted by $\vec{r}_1$ is where the acoustic pressure from the transducer is measured by a small point hydrophone. A voltage excitation of the transducer with a delta function will give rise to a pressure field that is measured by the hydrophone. The measured response is the acoustic impulse response for this particular system with the given set-up. Moving the transducer or the hydrophone to a new position will give a different response. Moving the hydrophone closer to the transducer surface will often increase the signal[2], and moving it away from the center axis of the transducer will often diminish it. Thus, the impulse response depends on the relative position of both the transmitter and receiver $(\vec{r}_2 - \vec{r}_1)$ and hence it is called a spatial impulse response.

A perception of the sound field for a fixed time instance can be obtained by employing Huygens' principle in which every point on the radiating surface is the origin of an outgoing spherical wave. This is illustrated in Fig. 1.13. Each of the outgoing spherical waves are given by

$$p_s(\vec{r}_1,t) = k_p \frac{\delta\left(t - \frac{|\vec{r}_2-\vec{r}_1|}{c}\right)}{|\vec{r}_2-\vec{r}_1|} = k_p \frac{\delta\left(t - \frac{|r|}{c}\right)}{|r|} \tag{1.26}$$

where $\vec{r}_1$ indicates the point in space, $\vec{r}_2$ is the point on the transducer surface, k_p is a constant, and t is the time for the snapshot of the spatial distribution of the pressure. The spatial impulse response is then found by observing the pressure waves at a fixed position in space over time by having all the spherical waves pass the point of observation and summing them. Being on the acoustical axis of the transducer gives a short response whereas an off-axis point yields a longer impulse response as shown in Fig. 1.13.

1.5.2 Basic theory

In this section the exact expression for the spatial impulse response will more formally be derived. The basic setup is shown in Fig. 1.14. The triangular shaped aperture is placed in an infinite, rigid baffle on which the velocity normal to the plane is zero, except at the aperture. The field point is denoted by $\vec{r}_1$ and the aperture by $\vec{r}_2$. The pressure field generated by the

[2]This is not always the case. It depends on the focusing of the transducer. Moving closer to the transducer but away from its focus will decrease the signal.

aperture is then found by the Rayleigh integral [9]

$$p(\vec{r}_1,t) = \frac{\rho_0}{2\pi}\int_S \frac{\frac{\partial v_n(\vec{r}_2,t-\frac{|\vec{r}_1-\vec{r}_2|}{c})}{\partial t}}{|\,\vec{r}_1-\vec{r}_2\,|}dS, \tag{1.27}$$

where v_n is the velocity normal to the transducer surface. The integral is a statement of Huygens' principle that the field is found by integrating the contributions from all the infinitesimally small area elements that make up the aperture. This integral formulation assumes linearity and propagation in a homogeneous medium without attenuation. Further, the radiating aperture is assumed flat, so no re-radiation from scattering and reflection takes place. Exchanging the integration and the partial derivative, the integral can be written as

$$p(\vec{r}_1,t) = \frac{\rho_0}{2\pi}\frac{\partial\int_S \frac{v_n(\vec{r}_2,t-\frac{|\vec{r}_1-\vec{r}_2|}{c})}{|\,\vec{r}_1-\vec{r}_2\,|}dS}{\partial t}. \tag{1.28}$$

It is convenient to introduce the velocity potential ψ that satisfies the equations [10]

$$\begin{aligned} \vec{v}(\vec{r},t) &= -\nabla\psi(\vec{r},t) \\ p(\vec{r},t) &= \rho_0\frac{\partial\psi(\vec{r},t)}{\partial t}. \end{aligned} \tag{1.29}$$

Then only a scalar quantity need to be calculated and all field quantities can be derived from it. The surface integral is then equal to the velocity potential:

$$\psi(\vec{r}_1,t) = \int_S \frac{v_n(\vec{r}_2,t-\frac{|\vec{r}_1-\vec{r}_2|}{c})}{2\pi\,|\,\vec{r}_1-\vec{r}_2\,|}dS \tag{1.30}$$

The excitation pulse can be separated from the transducer geometry by introducing a time convolution with a delta function as

$$\psi(\vec{r}_1,t) = \int_S\int_T \frac{v_n(\vec{r}_2,t_2)\delta(t-t_2-\frac{|\vec{r}_1-\vec{r}_2|}{c})}{2\pi\,|\,\vec{r}_1-\vec{r}_2\,|}dt_2dS, \tag{1.31}$$

where δ is the Dirac delta function.

Assume now that the surface velocity is uniform over the aperture making it independent of $\vec{r}_2$, then:

$$\psi(\vec{r}_1,t) = v_n(t) * \int_S \frac{\delta(t-\frac{|\vec{r}_1-\vec{r}_2|}{c})}{2\pi\,|\,\vec{r}_1-\vec{r}_2\,|}dS, \tag{1.32}$$

where $*$ denotes convolution in time. The integral in this equation

$$h(\vec{r}_1,t) = \int_S \frac{\delta(t-\frac{|\vec{r}_1-\vec{r}_2|}{c})}{2\pi\,|\,\vec{r}_1-\vec{r}_2\,|}dS \tag{1.33}$$

is called the spatial impulse response and characterizes the three-dimensional extent of the field for a particular transducer geometry. Note that this is a function of the relative position between the aperture and the field.

Using the spatial impulse response the pressure is written as

$$p(\vec{r}_1,t) = \rho_0 \frac{\partial v_n(t)}{\partial t} * h(\vec{r}_1,t) \tag{1.34}$$

which equals the emitted pulsed pressure for any kind of surface vibration $v_n(t)$. The continuous wave field can be found from the Fourier transform of (1.34). The received response for a collection of scatterers can also be found from the spatial impulse response [11], [12]. Thus, the calculation of the spatial impulse response makes it possible to find all ultrasound fields of interest.

1.5.3 Geometric considerations

The calculation of the spatial impulse response assumes linearity and any complex-shaped transducer can therefore be divided into smaller apertures and the response can be found by adding the responses from the sub-apertures. The integral is, as mentioned before, a statement of Huygens' principle of summing contributions from all areas of the aperture.

An alternative interpretation is found by using the acoustic reciprocity theorem [5]. This states that: "If in an unchanging environment the locations of a small source and a small receiver are interchanged, the received signal will remain the same." Thus, the source and receiver can be interchanged. Emitting a spherical wave from the field point and finding the wave's intersection with the aperture also yields the spatial impulse response. The situation is depicted in Fig. 1.15, where an outgoing spherical wave is emitted from the origin of the coordinate system. The dashed curves indicate the circles from the projected spherical wave.

The calculation of the impulse response is then facilitated by projecting the field point onto the plane of the aperture. The task is thereby reduced to a two-dimensional problem and the field point is given as a (x,y) coordinate set and a height z above the plane. The three-dimensional spherical waves are then reduced to circles in the $x-y$ plane with the origin at the position of the projected field point as shown in Fig. 1.16.

The spatial impulse response is, thus, determined by the relative length of the part of the arc that intersects the aperture. Thereby it is the crossing of the projected spherical waves with the edges of the aperture that determines the spatial impulse responses. This fact is used for deriving equations for the spatial impulse responses in the next section.

1.5.4 Calculation of spatial impulse responses

The spatial impulse response is found from the Rayleigh integral derived earlier

$$h(\vec{r}_1,t) = \int_S \frac{\delta(t - \frac{|\vec{r}_1 - \vec{r}_2|}{c})}{2\pi \mid \vec{r}_1 - \vec{r}_2 \mid} dS \tag{1.35}$$

The task is to project the field point onto the plane coinciding with the aperture, and then find the intersection of the projected spherical wave (the circle) with the active aperture as shown in Fig. 1.16.

Rewriting the integral into polar coordinates gives:

$$h(\vec{r}_1,t) = \int_{\Theta_1}^{\Theta_2} \int_{d_1}^{d_2} \frac{\delta(t - \frac{R}{c})}{2\pi R} r\, dr\, d\Theta \tag{1.36}$$

where r is the radius of the projected circle and R is the distance from the field point to the aperture given by $R^2 = r^2 + z_p^2$. Here z_p is the field point height above the $x-y$ plane of the aperture. The projected distances d_1, d_2 are determined by the aperture and are the distance closest to and furthest away from the aperture, and Θ_1, Θ_2 are the corresponding angles for a given time (see Fig. 1.17).

Introducing the substitution $2RdR = 2rdr$ gives

$$h(\vec{r}_1,t) = \frac{1}{2\pi} \int_{\Theta_1}^{\Theta_2} \int_{R_1}^{R_2} \delta(t - \frac{R}{c})\, dR\, d\Theta \tag{1.37}$$

The variables R_1 and R_2 denote the edges closest to and furthest away from the field point. Finally using the substitution $t' = R/c$ gives

$$h(\vec{r}_1,t) = \frac{c}{2\pi} \int_{\Theta_1}^{\Theta_2} \int_{t_1}^{t_2} \delta(t - t') dt' d\Theta \tag{1.38}$$

For a given time instance the contribution along the arc is constant and the integral gives

$$h(\vec{r}_1,t) = \frac{\Theta_2 - \Theta_1}{2\pi} c \tag{1.39}$$

when assuming the circle arc is only intersected once by the aperture. The angles Θ_1 and Θ_2 are determined by the intersection of the aperture and the projected spherical wave, and the spatial impulse response is, thus, solely determined by these intersections, when no apodization of the aperture is used. The response can therefore be evaluated by keeping track of the intersections as a function of time.

1.5.5 Examples of spatial impulse responses

The first example shows the spatial impulse responses from a 3×5 mm rectangular element for different spatial positions 5 mm from the front face of the transducer. The responses are found from the center of the rectangle ($y = 0$) and out in steps of 2 mm in the x direction to 6 mm away from the center of the rectangle. A schematic diagram of the situation is shown in Fig. 1.18 for the on-axis response. The impulse response is zero before the first spherical wave reaches the aperture. Then the response stays constant at a value of c. The first edge of the aperture is met, and the response drops of. The decrease with time is increased, when the next edge of the aperture is reached and the response becomes zero when the projected spherical waves all are outside the area of the aperture.

A plot of the results for the different lateral field positions is shown in Fig. 1.19. It can be seen how the spatial impulse response changes as a function of relative position to the aperture.

The second example shows the response from a circular, flat transducer. Two different cases are shown in Fig. 1.20. The top graph shows the traditional spatial impulse response when no apodization is used, so that the aperture vibrates as a piston. The field is calculated 10 mm from the front face of the transducer starting at the center axis of the aperture. Twenty-one responses for lateral distance of 0 to 20 mm off axis are then shown. The same calculation is repeated in the bottom graph, when a Gaussian apodization has been imposed on the aperture. The vibration amplitude is a factor of $1/\exp(4)$ less at the edges of the aperture than at the center. It is seen how the apodization reduces some of the sharp discontinuities in the spatial impulse response, which can reduce the sidelobes of the field.

1.5.6 Pulse-echo fields

The scattered field and received signal by the transducer can also be described using the spatial impulse response. The received signal from the transducer is [12]:

$$p_r(\vec{r},t) = v_{pe}(t) \underset{t}{\star} f_m(\vec{r}) \underset{r}{\star} h_{pe}(\vec{r},t) \tag{1.40}$$

where $\underset{r}{\star}$ denotes spatial convolution and $\underset{t}{\star}$ denotes temporal convolution. v_{pe} is the pulse-echo impulse, which includes the transducer excitation and the electro-mechanical impulse response during emission and reception of the pulse. f_m accounts for the inhomogeneities in the tissue due to density and speed of sound perturbations, which give rise to the scattered signal. h_{pe} is the pulse-echo spatial impulse response that relates the transducer geometry to the spatial extent of the scattered field. Explicitly written out these terms are:

$$v_{pe}(t) = \frac{\rho}{2c^2} E_m(t) \underset{t}{\star} \frac{\partial^3 v(t)}{\partial t^3}, \qquad f_m(\vec{r}_1) = \frac{\Delta\rho(\vec{r})}{\rho} - \frac{2\Delta c(\vec{r})}{c}, \qquad h_{pe}(\vec{r},t) = h_t(\vec{r},t) * h_r(\vec{r},t) \tag{1.41}$$

Here $\Delta\rho$ are the perturbations in density and Δc in speed of sound, and $h_t(\vec{r},t)$ and $h_r(\vec{r},t)$ are the spatial impulse responses for the transmitting and receiving apertures, respectively. $E_m(t)$ is the electro-mechanical impulse response of the transducer during reception. So the received response can be calculated by finding the spatial impulse response for the transmitting and receiving transducer and then convolving with the impulse response of the transducer. A single RF line in an image can be calculated by summing the response from a collection of scatterers in which the scattering strength is determined by the density and speed of sound perturbations in the tissue. Homogeneous tissue can thus be made from a collection of randomly placed scatterers with a scattering strength with a Gaussian distribution, where the variance of the distribution is determined by the backscattering cross-section of the particular tissue.

1.6 Fields from array transducers

Most modern scanners use arrays for generating and receiving the ultrasound fields. These fields are quite simple to calculate, when the spatial impulse response for a single element is known. This is the approach used in the Field II program [13], and this section will extend the spatial impulse response to multi-element transducers and will elaborate on some of the features derived for the fields in Section 1.4.

Since the ultrasound propagation is assumed to be linear, the individual spatial impulse responses can simply be added. If $h_e(\vec{r}_p,t)$ denotes the spatial impulse response for the element at position $\vec{r}_i$ and the field point $\vec{r}_p$, then the spatial impulse response for the array is

$$h_a(\vec{r}_p,t) = \sum_{i=0}^{N-1} h_e(\vec{r}_i,\vec{r}_p,t), \tag{1.42}$$

assuming all N elements to be identical.

Let us assume that the elements are very small and the field point is far away from the array, so h_e is a Dirac function. Then

$$h_a(\vec{r}_p,t) = \frac{k}{R_p} \sum_{i=0}^{N-1} \delta(t - \frac{|\vec{r}_i - \vec{r}_p|}{c}) \tag{1.43}$$

when $R_p = |\vec{r}_a - \vec{r}_p|$, k is a constant of proportionality, and $\vec{r}_a$ is the position of the array. Thus, h_a is a train of Dirac pulses. If the spacing between the elements is d_x, then

$$h_a(\vec{r}_p,t) = \frac{k}{R_p} \sum_{i=0}^{N-1} \delta\left(t - \frac{|\vec{r}_a + id_x\vec{r}_e - \vec{r}_p|}{c}\right), \tag{1.44}$$

where $\vec{r}_e$ is a unit vector pointing in the direction along the elements. The geometry is shown in Fig. 1.21.

The difference in arrival time between elements far from the transducer is

$$\Delta t = \frac{d_x \sin\Theta}{c}. \tag{1.45}$$

The spatial impulse response is, thus, a series of Dirac pulses separated by Δt.

$$h_a(\vec{r}_p, t) \approx \frac{k}{R_p} \sum_{i=0}^{N-1} \delta\left(t - \frac{R_p}{c} - i\Delta t\right). \tag{1.46}$$

The time between the Dirac pulses and the shape of the excitation determines whether signals from individual elements add or cancel out. If the separation in arrival times corresponds to exactly one or more periods of a sine wave, then they are in phase and add constructively. Thus, peaks in the response are found for

$$n\frac{1}{f} = \frac{d_x \sin\Theta}{c}. \tag{1.47}$$

The main lobe is found for $\Theta = 0$ and the next maximum in the response is found for

$$\Theta = \arcsin\left(\frac{c}{f d_x}\right) = \arcsin\left(\frac{\lambda}{d_x}\right). \tag{1.48}$$

For a 3 MHz array with an element spacing of 1 mm, this amounts to $\Theta = 31^\circ$, which will be within the image plane. The received response is, thus, affected by scatterers positioned 31° off the image axis, and they will appear in the lines acquired as grating lobes. The first grating lobe can be moved outside the image plane, if the elements are separated by less than a wavelength. Usually, half a wavelength separation is desirable, as this gives some margin for a broad-band pulse and beam steering.

The beam pattern as a function of angle for a particular frequency can be found by Fourier transforming h_a

$$\begin{aligned} H_a(f) &= \frac{k}{R_p} \sum_{i=0}^{N-1} \exp\left(-j2\pi f\left(\frac{R_p}{c} + i\frac{d_x \sin\Theta}{c}\right)\right) \\ &= \exp(-j2\pi f \frac{R_p}{c}) \frac{k}{R_p} \sum_{i=0}^{N-1} \exp\left(-j2\pi f \frac{d_x \sin\Theta}{c}\right)^i \\ &= \frac{\sin(\pi f \frac{d_x \sin\Theta}{c} N)}{\sin(\pi f \frac{d_x \sin\Theta}{c})} \exp(-j\pi f(N-1)\frac{d_x \sin\Theta}{c}) \frac{k}{R_p} \exp(-j2\pi f \frac{R_p}{c}). \end{aligned} \tag{1.49}$$

The terms $\exp(-j2\pi f \frac{R_p}{c})$ and $\exp(-j\pi f(N-1)\frac{d_x \sin\Theta}{c})$ are constant phase shifts and play no role for the amplitude of the beam profile. Thus, the amplitude of the beam profile is

$$|H_a(f)| = \left| \frac{k}{R_p} \frac{\sin(N\pi \frac{d_x}{\lambda} \sin\Theta)}{\sin(\pi \frac{d_x}{\lambda} \sin\Theta)} \right|, \tag{1.50}$$

which is consistent with the previously derived result.

Several factors change the beam profile for real, pulsed arrays compared with the analysis given here. First, the elements are not points, but rather are rectangular elements with an off-axis spatial impulse response markedly different from a Dirac pulse. Therefore, the spatial impulse responses of the individual elements will overlap and exact cancellation or addition will not take place. Second, the excitation pulse is broad band, which again influences the sidelobes. The influence of these factors is shown in a set of simulations in the next section.

1.7 Examples of ultrasound fields

The field examples are generated using computer phantoms and the Field II simulation program, that is based on the spatial impulse approach [14, 13].

The first synthetic phantom consists of a number of point targets placed with a distance of 5 mm starting at 15 mm from the transducer surface. A linear sweep image of the points is then made and the resulting image is compressed to show a 40 dB dynamic range. This phantom is suited for showing the spatial variation of the point spread function for a particular transducer, focusing, and apodization scheme.

Twelve examples using this phantom are shown in Fig. 1.22. The top graphs show imaging without apodization and the bottom graphs show images when a Hanning window is used for apodization in both transmit and receive. A 128 elements transducer with a nominal frequency of 3 MHz was used. The element height was 5 mm, the width was a wavelength and the kerf 0.1 mm. The excitation of the transducer consisted of 2 periods of a 3 MHz sinusoid with a Hanning weighting, and the impulse response of both the emit and receive aperture was also a two cycle, Hanning weighted pulse. In the graphs A – C, 64 of the transducer elements were used for imaging, and the scanning was done by translating the 64 active elements over the aperture and focusing in the proper points. In graph D and E 128 elements were used and the imaging was done solely by moving the focal points.

Graph A uses only a single focal point at 60 mm for both emission and reception. B also uses reception focusing at every 20 mm starting from 30 mm. Graph C further adds emission focusing at 10, 20, 40, and 80 mm. D applies the same focal zones as C, but uses 128 elements in the active aperture.

The focusing scheme used for E and F applies a new receive profile for each 2 mm. For analog beamformers this is a small zone size. For digital beamformers it is a large zone size. Digital beamformer can be programmed for each sample and thus a ”continuous” beamtracking can be obtained. In imaging systems focusing is used to obtain high detail resolution and high contrast resolution preferably constant for all depths. This is not possible, so compromises must be made. As an example figure F shows the result for multiple transmit zones and receive

zones, like E, but now a restriction is put on the active aperture. The size of the aperture is controlled to have a constant F-number (depth of focus in tissue divided by width of aperture), 4 for transmit and 2 for receive, by dynamic apodization. This gives a more homogeneous point spread function throughout the full depth. Especially for the apodized version. Still it can be seen that the composite transmit can be improved in order to avoid the increased width of the point spread function at e.g. 40 and 60 mm.

The next phantom consists of a collection of point targets, five cyst regions, and five highly scattering regions. This can be used for characterizing the contrast-lesion detection capabilities of an imaging system. The scatterers in the phantom are generated by finding their random position within a $60 \times 40 \times 15$ mm cube, and then ascribe a Gaussian distributed amplitude to the scatterers. If the scatterer resides within a cyst region, the amplitude is set to zero. Within the highly scattering region the amplitude is multiplied by 10. The point targets has a fixed amplitude of 100, compared to the standard deviation of the Gaussian distributions of 1. A linear scan of the phantom was done with a 192 element transducer, using 64 active elements with a Hanning apodization in transmit and receive. The element height was 5 mm, the width was a wavelength and the kerf 0.05 mm. The pulses where the same as used for the point phantom mentioned above. A single transmit focus was placed at 60 mm, and receive focusing was done at 20 mm intervals from 30 mm from the transducer surface. The resulting image for 100,000 scatterers is shown in Fig. 1.23. A homogeneous speckle pattern is seen along with all the features of the phantom.

1.8 Summary

Modern ultrasound scanners has attained a very high image quality through the use of digital beamforming. The delays on the individual transducer elements and their relative weight or apodization is changed continuously as a function of depth. This yields near perfect focused images for all depths and has increased the contrast in the displayed image, thus, benefitting the diagnostic value of ultrasonic imaging. The development of the focusing strategies is nearly exclusively based on linear acoustics, and the high success of the approach attest to the validity of using linear acoustics. It is, thus, appropriate to characterize the medical ultrasound systems using linear acoustics. This chapter has developed a complete linear description of all the fields encountered in medical ultrasound. The various imaging methods were described, and then the concept of spatial impulse responses was developed. This could be used for describing both emitted and pulse-echo fields for both pulse emission and continuous wave systems using linear systems theory. Examples of the influence of digital beamforming and apodization were also shown.

Bibliography

[1] S. A. Goss, R. L. Johnston, and F. Dunn. Comprehensive compilation of empirical ultrasonic properties of mammalian tissues. *J. Acoust. Soc. Am.*, 64:423–457, 1978.

[2] S. A. Goss, R. L. Johnston, and F. Dunn. Compilation of empirical ultrasonic properties of mammalian tissues II. *J. Acoust. Soc. Am.*, 68:93–108, 1980.

[3] J. A. Jensen. *Estimation of Blood Velocities Using Ultrasound: A Signal Processing Approach*. Cambridge University Press, New York, 1996.

[4] R. F. Wagner, S. W. Smith, J. M. Sandrick, and H. Lopez. Statistics of speckle in ultrasound B-scans. *IEEE Trans. Son. Ultrason.*, 30:156–163, 1983.

[5] L. E. Kinsler, A. R. Frey, A. B. Coppens, and J. V. Sanders. *Fundamentals of Acoustics*. John Wiley & Sons, New York, third edition, 1982.

[6] G. E. Tupholme. Generation of acoustic pulses by baffled plane pistons. *Mathematika*, 16:209–224, 1969.

[7] P. R. Stepanishen. The time-dependent force and radiation impedance on a piston in a rigid infinite planar baffle. *J. Acoust. Soc. Am.*, 49:841–849, 1971.

[8] P. R. Stepanishen. Transient radiation from pistons in an infinte planar baffle. *J. Acoust. Soc. Am.*, 49:1629–1638, 1971.

[9] A. D. Pierce. *Acoustics, An Introduction to Physical Principles and Applications*. Acoustical Society of America, New York, 1989.

[10] P. M. Morse and K. U. Ingard. *Theoretical Acoustics*. McGraw-Hill, New York, 1968.

[11] P. R. Stepanishen. Pulsed transmit/receive response of ultrasonic piezoelectric transducers. *J. Acoust. Soc. Am.*, 69:1815–1827, 1981.

[12] J. A. Jensen. A model for the propagation and scattering of ultrasound in tissue. *J. Acoust. Soc. Am.*, 89:182–191, 1991a.

[13] J. A. Jensen. Field: A program for simulating ultrasound systems. *Med. Biol. Eng. Comp.*, 10th Nordic-Baltic Conference on Biomedical Imaging, Vol. 4, Supplement 1, Part 1:351–353, 1996b.

[14] J. A. Jensen and N. B. Svendsen. Calculation of pressure fields from arbitrarily shaped, apodized, and excited ultrasound transducers. *IEEE Trans. Ultrason., Ferroelec., Freq. Contr.*, 39:262–267, 1992.

[15] M. J. Haney and W. D. O'Brien. Temperature dependency of ultrasonic propagation properties in biological materials. In J. F. Greenleaf, editor, *Tissue Characterization with Ultrasound*. CRC Press, Boca Raton, Fla., 1986.

Tables

Tissue	Attenuation dB/[MHz·cm]
Liver	0.6 – 0.9
Kidney	0.8 – 1.0
Spleen	0.5 – 1.0
Fat	1.0 – 2.0
Blood	0.17 – 0.24
Plasma	0.01
Bone	16.0 – 23.0

Table 1.1: Typical attenuation values for human tissue (assembled from the compilation in [15]).

Figures

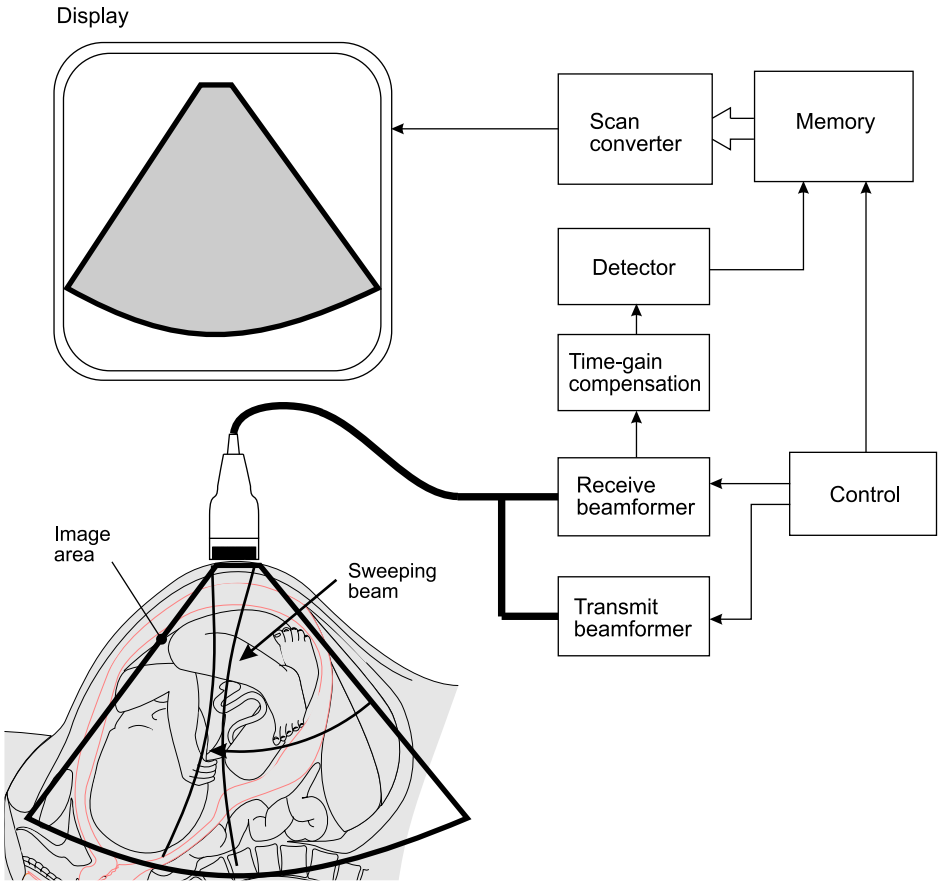

Figure 1.1: Real-time B-mode ultrasound imaging system.

Figure 1.2: Ultrasound image of a 13th week fetus. The markers at the border of the image indicate one centimeter.

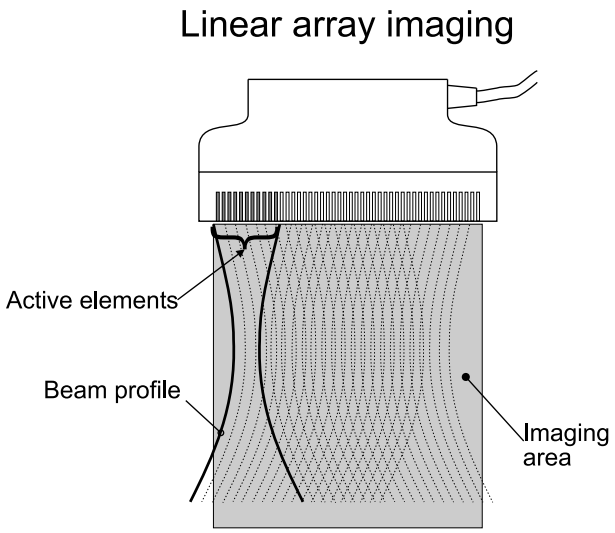

Figure 1.3: Linear array transducer for obtaining a rectangular cross-sectional image.

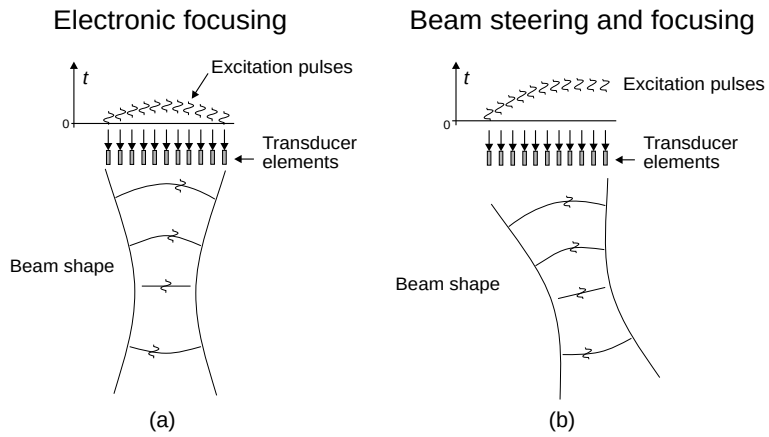

Figure 1.4: Electronic focusing and steering of an ultrasound beam.

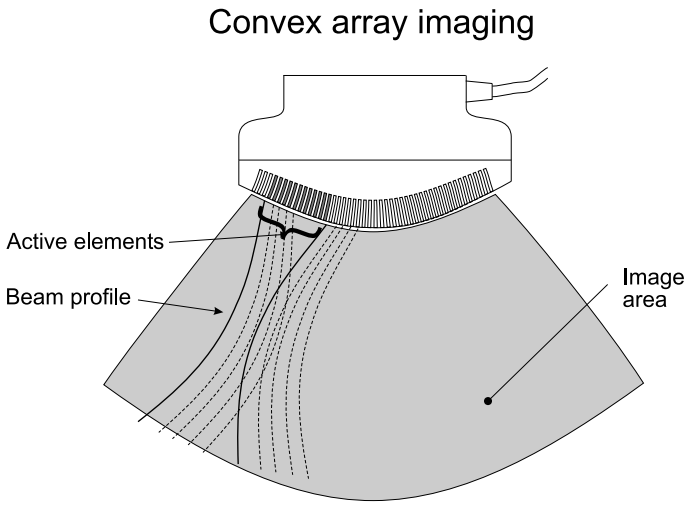

Figure 1.5: Convex array transducer for obtaining a polar cross-sectional image.

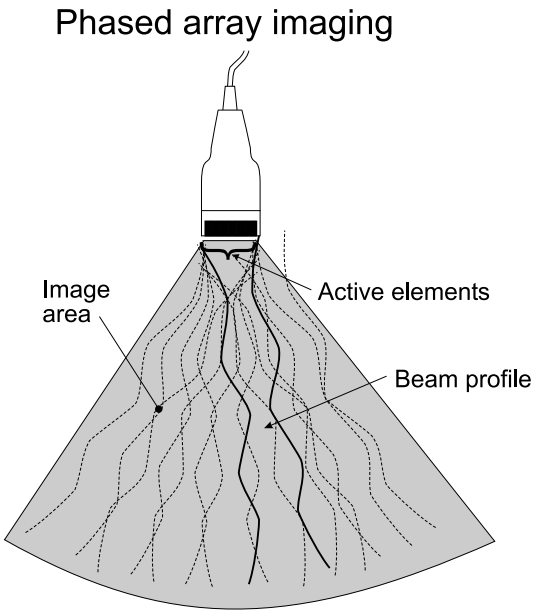

Figure 1.6: Phased array transducer for obtaining a polar cross-sectional image using a transducer with a small foot-print.

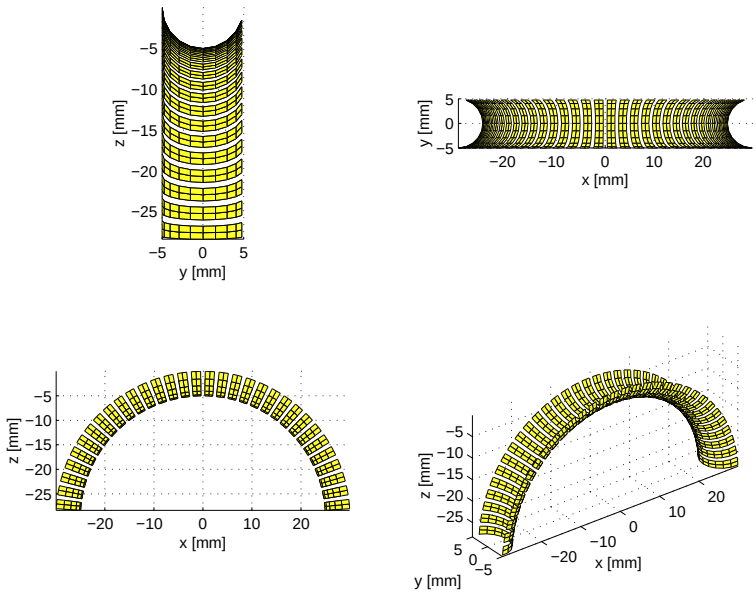

Figure 1.7: Elevation focused convex array transducer for obtaining a rectangular cross-sectional image, which is focused in the out-of-plane direction. The curvature in the elevation direction is exaggerated in the figure for illustration purposes.

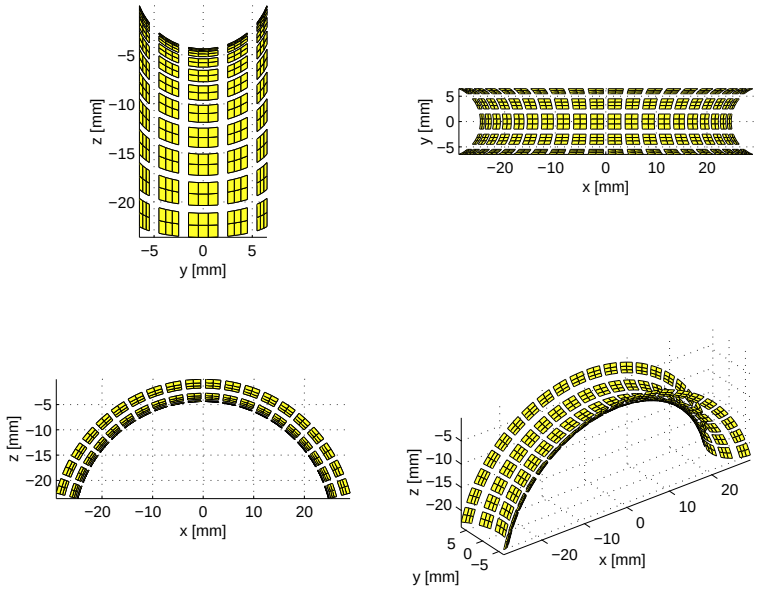

Figure 1.8: Elevation focused convex array transducer with element division in the elevation direction. The curvature in the elevation direction is exaggerated in the figure for illustration purposes.

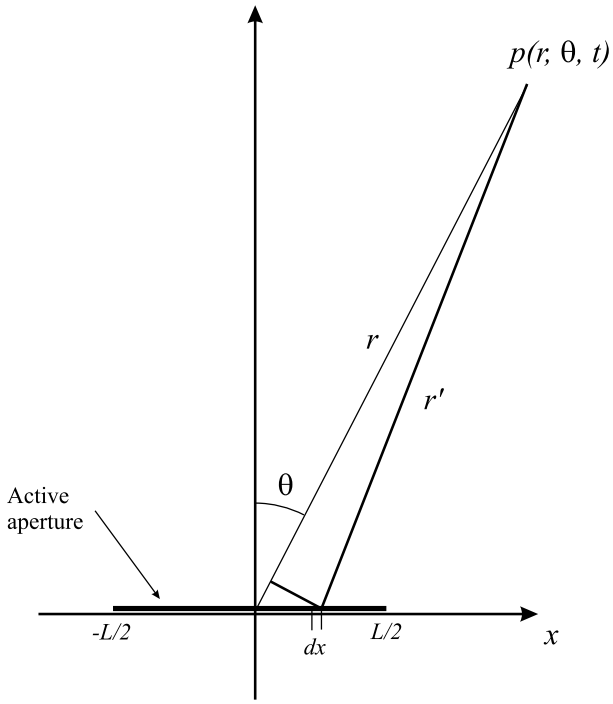

Figure 1.9: Geometry for line aperture.

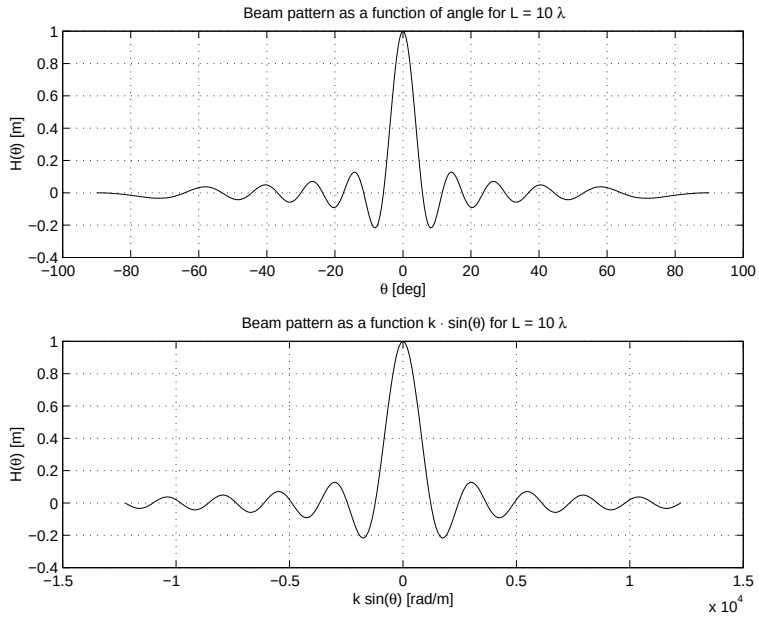

Figure 1.10: Angular beam pattern for a line aperture with a uniform aperture function as a function of angle (top) and as a function of $k\sin(\theta)$ (bottom).

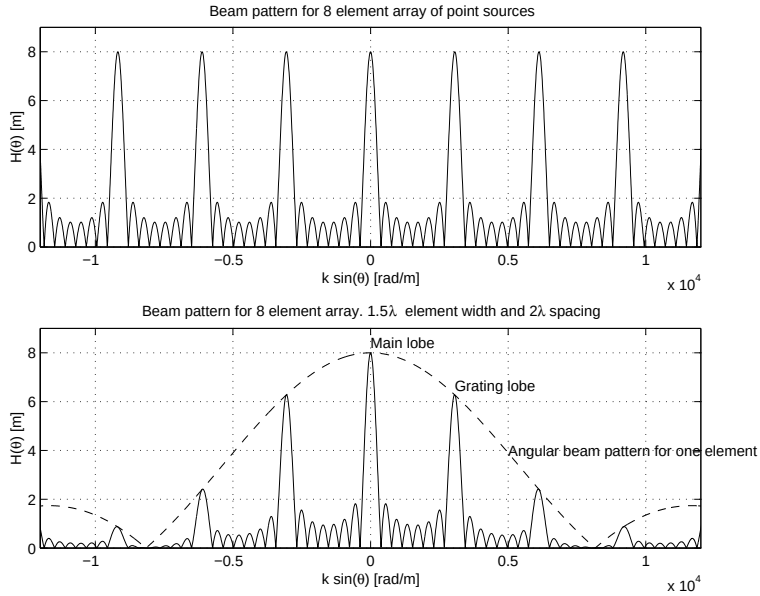

Figure 1.11: Grating lobes for array transducer consisting of 8 point elements (top) and of 8 elements with a size of 1.5λ (bottom). The pitch (or distance between the elements) is 2λ.

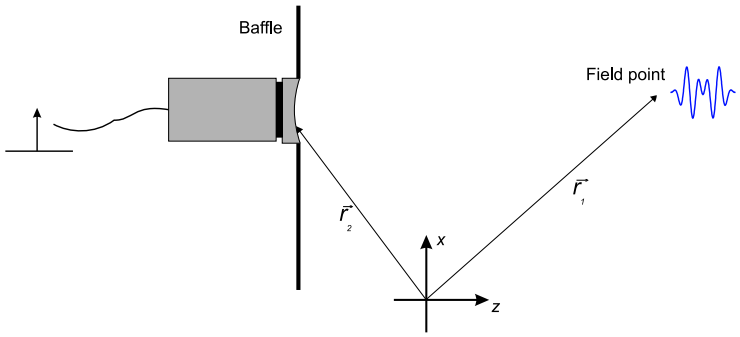

Figure 1.12: A linear acoustic system.

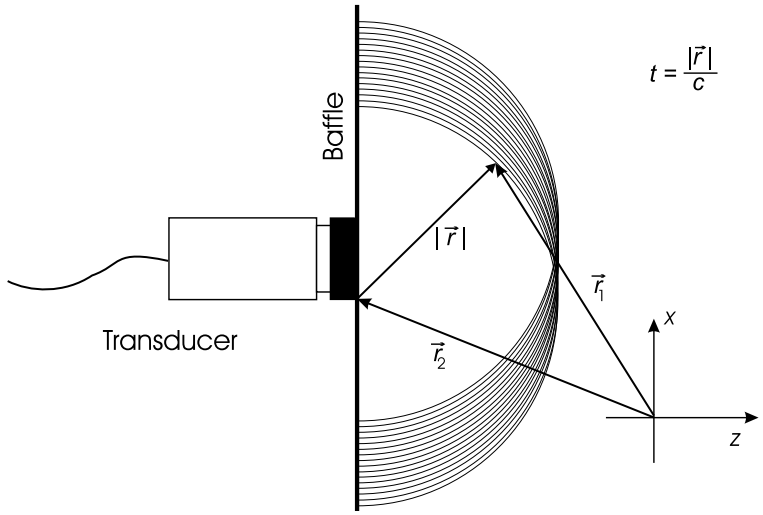

Figure 1.13: Illustration of Huygens' principle for a fixed time instance. A spherical wave with a radius of $|\vec{r}| = ct$ is radiated from each point on the aperture.

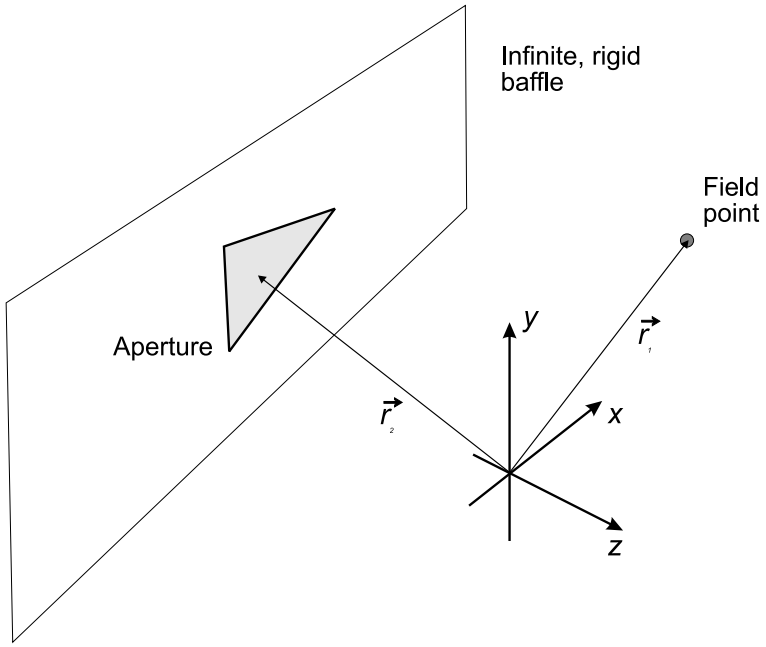

Figure 1.14: Position of transducer, field point, and coordinate system.

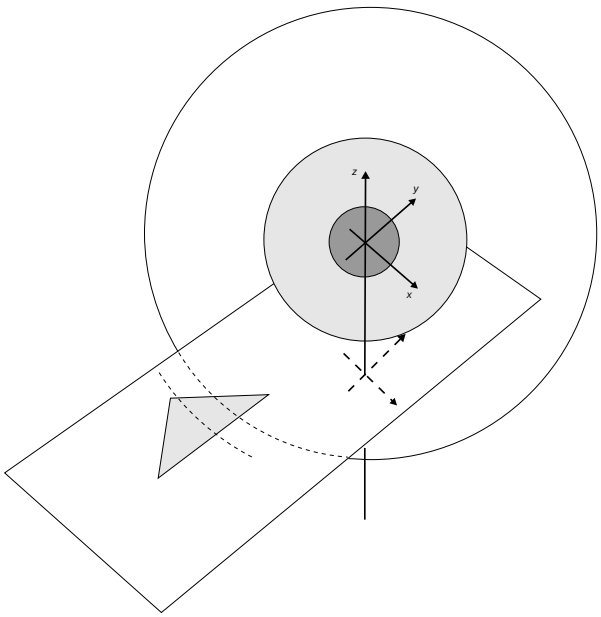

Figure 1.15: Emission of a spherical wave from the field point and its intersection of the aperture.

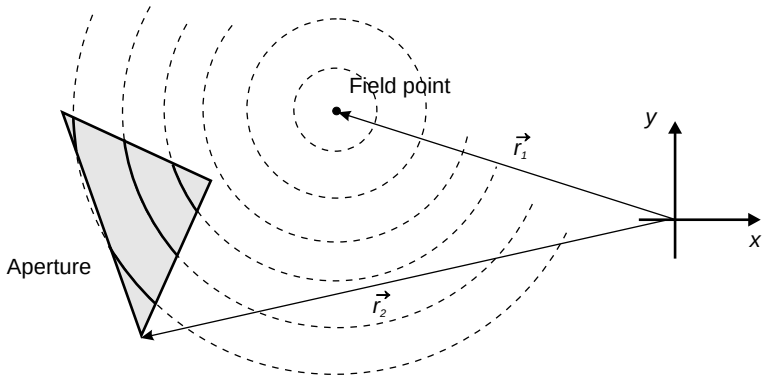

Figure 1.16: Intersection of spherical waves from the field point by the aperture, when the field point is projected onto the plane of the aperture.

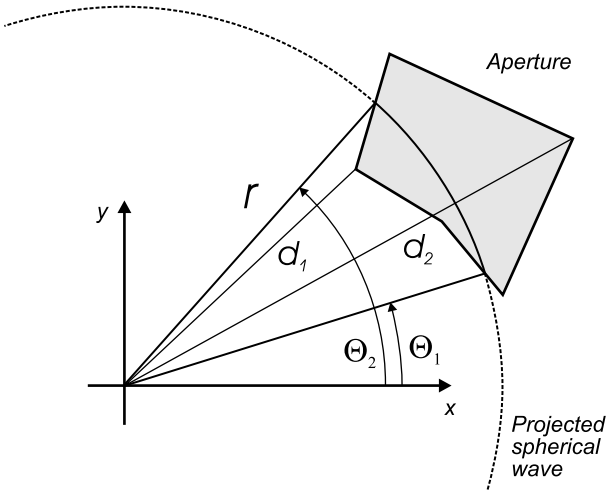

Figure 1.17: Definition of distances and angles in the aperture plan for evaluating the Rayleigh integral.

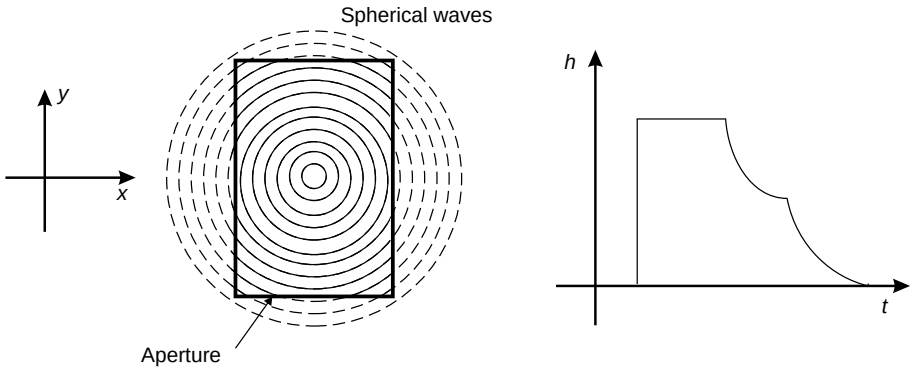

Figure 1.18: Schematic diagram of field from rectangular element.

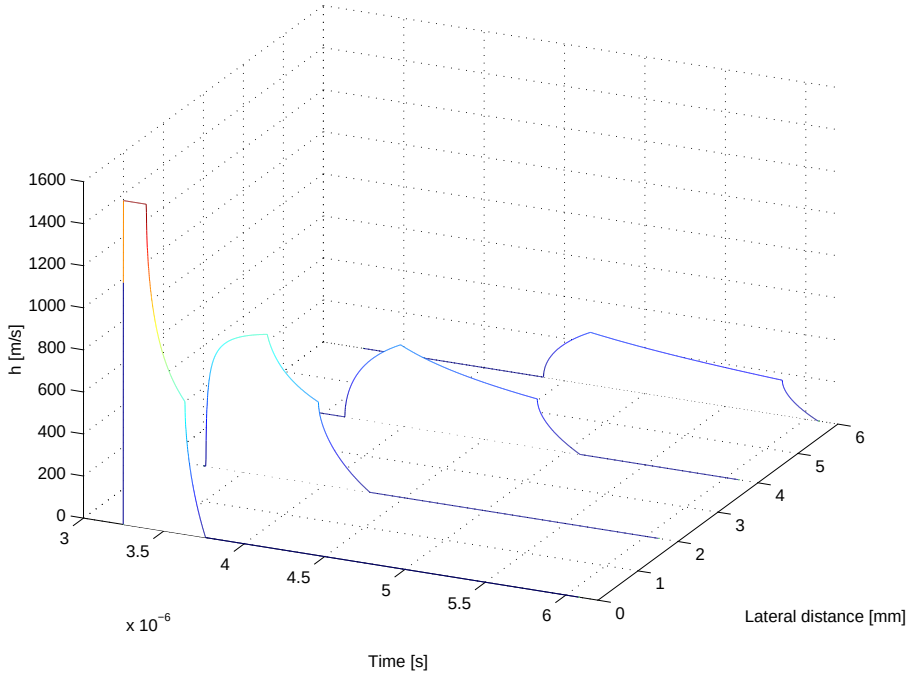

Figure 1.19: Spatial impulse response from a rectangular aperture of 4×5 mm at for different lateral positions.

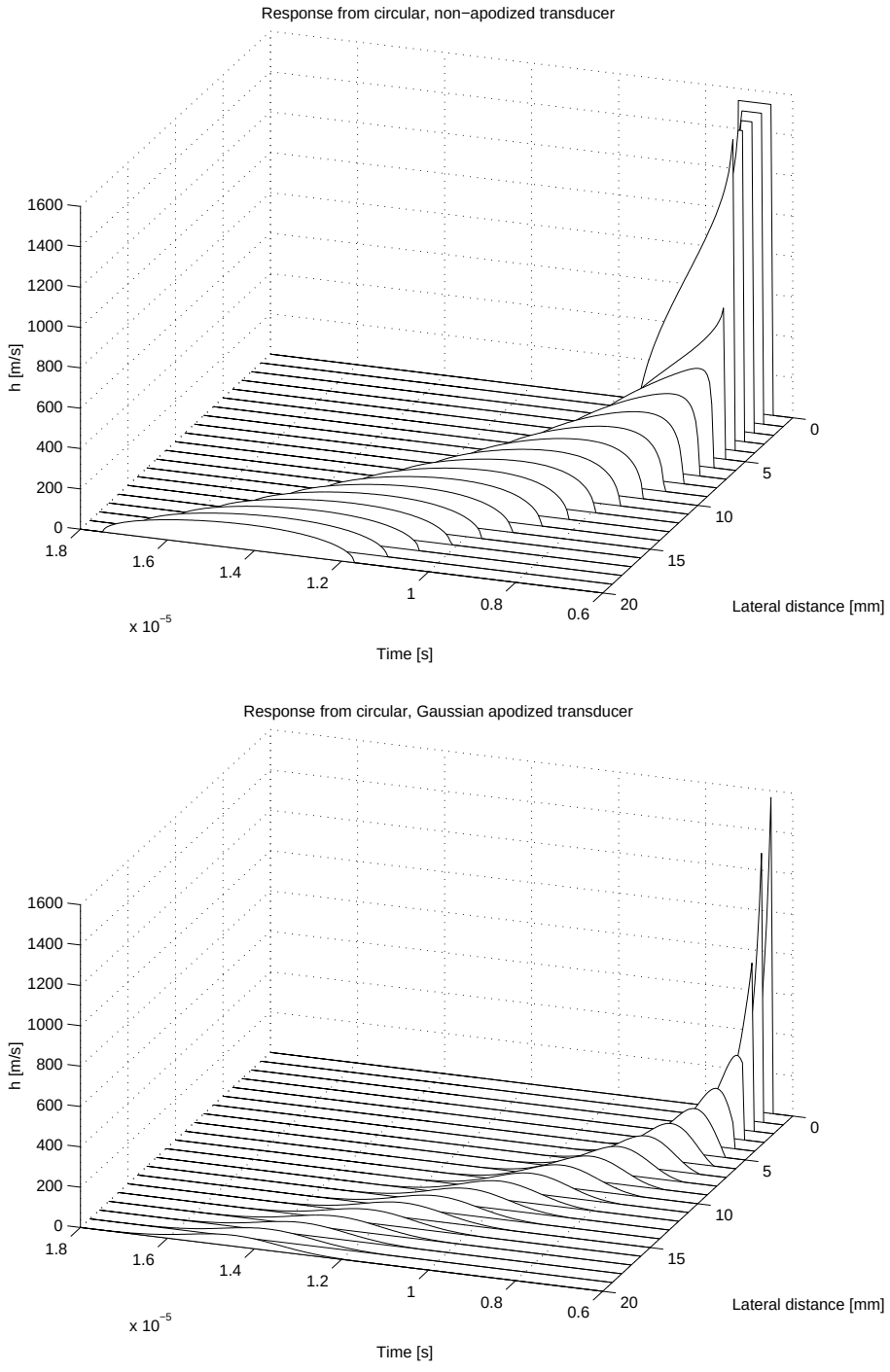

Figure 1.20: Spatial impulse response from a circular aperture. Graphs are shown without apodization of the aperture (top) and with a Gaussian apodization function (bottom). The radius of the aperture is 5 mm and the field is calculated 10 mm from the transducer surface.

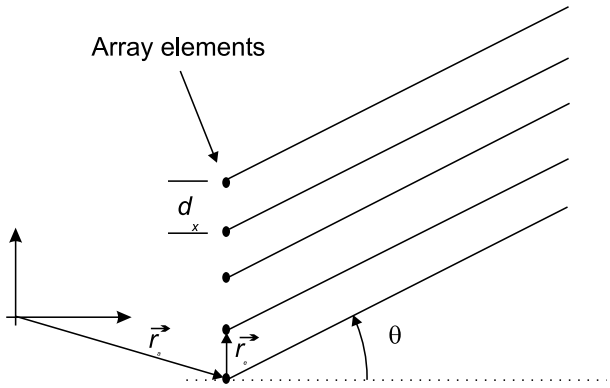

Figure 1.21: Geometry of linear array.

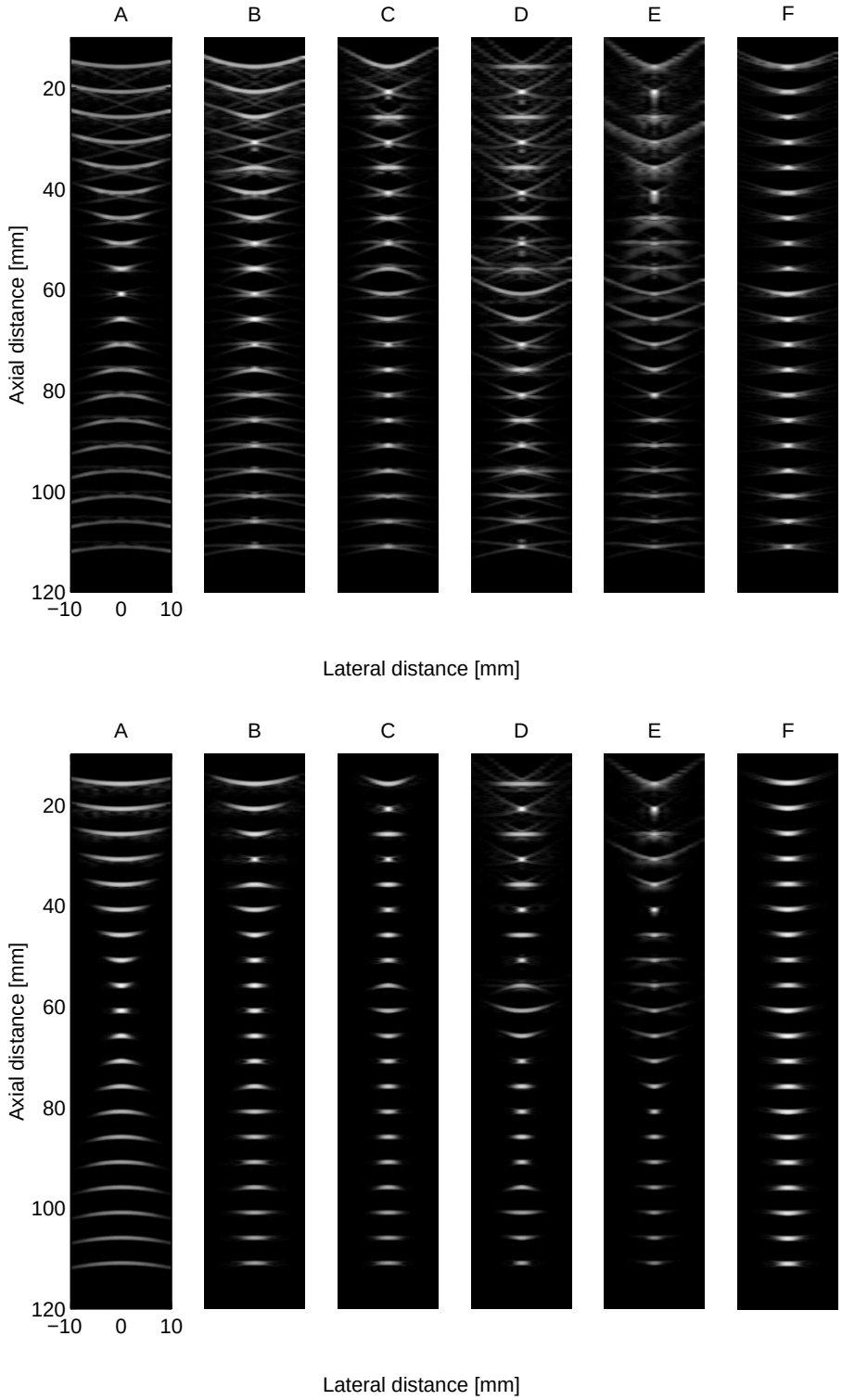

Figure 1.22: Point target phantom imaged for different set-up of transmit and receive focusing and apodization. See text for an explanation of the set-up.

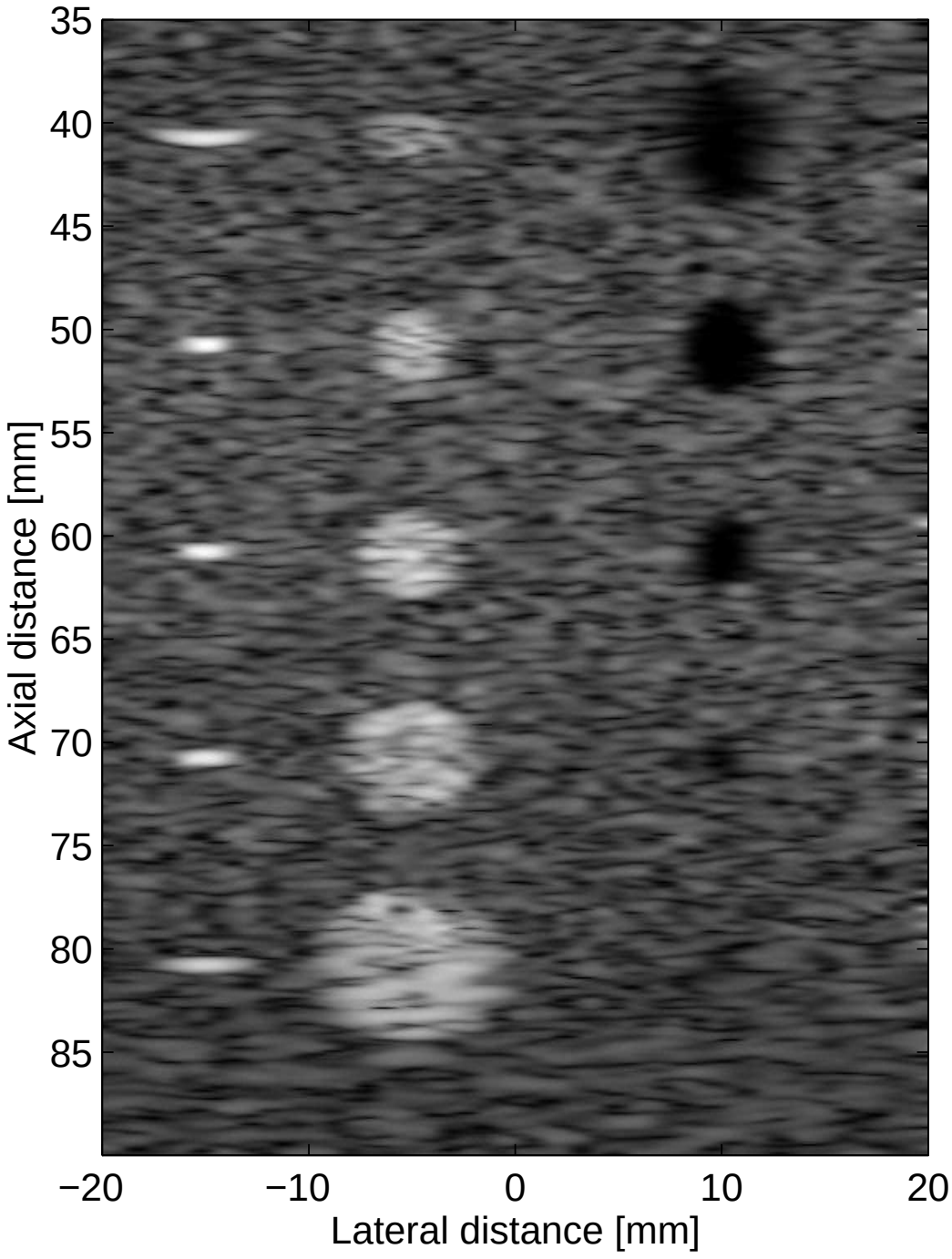

Figure 1.23: Computer phantom with point targets, cyst regions, and strongly reflecting regions.